High resolution magnetohydrodynamic simulation of black hole-neutron star merger: Mass ejection and short gamma ray bursts

Kenta Kiuchi,[1] Yuichiro Sekiguchi,[1,2] Koutarou Kyutoku,[3] Masaru Shibata,[1]
Keisuke Taniguchi,[4,6] and Tomohide Wada[5]

[1]*Yukawa Institute for Theoretical Physics, Kyoto University, Kyoto 606-8502, Japan*
[2]*Department of Physics, Toho University, Funabashi, Chiba 274-8510, Japan*
[3]*Interdisciplinary Theoretical Science (iTHES) Research Group, RIKEN, Wako, Saitama 351-0198, Japan*
[4]*Department of Physics, University of the Ryukyus, Nishihara, Okinawa 903-0213, Japan*
[5]*Tsukuba University of Technology, 4-3-15 Amakubo, Tsukuba 305-8520, Japan*
[6]*Graduate School of Arts and Sciences, University of Tokyo, Komaba, Meguro, Tokyo 153-8902, Japan*

We report results of a high resolution numerical-relativity simulation for the merger of black hole-magnetized neutron star binaries on Japanese supercomputer "K." We focus on a binary that is subject to tidal disruption and subsequent formation of a massive accretion torus. We find the launch of thermally driven torus wind, subsequent formation of a funnel wall above the torus and a magnetosphere with collimated poloidal magnetic field, and high Blandford-Znajek luminosity. We show for the first time this picture in a self-consistent simulation. The turbulencelike motion induced by the nonaxisymmetric magnetorotational instability as well as the Kelvin-Helmholtz instability inside the accretion torus works as an agent to drive the mass accretion and converts the accretion energy to thermal energy, which results in the generation of a strong wind. By an in-depth resolution study, we reveal that high resolution is essential to draw such a picture. We also discuss the implication for the r-process nucleosynthesis, the radioactively powered transient emission, and short gamma ray bursts.

I. INTRODUCTION

The merger of a black hole (BH) and a neutron star (NS) is one of the most promising sources of gravitational waves [1–3]. It could be also one of the strongest high-energy phenomena in the Universe, if the NS is tidally disrupted by the companion BH before the onset of the merger. Previous numerical-relativity simulations [4–15] have shown that after tidal disruption, a system composed of a BH and a torus is formed. This system could be the central engine of short gamma ray bursts (sGRBs) [16]. It is also found that during tidal disruption, an appreciable amount of mass is ejected [7,8,10,11]. Such ejecta, which should be neutron rich, will subsequently produce heavy elements via r-process nucleosynthesis [17]. The produced unstable heavy elements will subsequently decay, heat up the ejecta, and shine [18]. Such an electromagnetic signal could be an electromagnetic counterpart to detected gravitational waves [19–27].

These facts motivate us to perform physically reliable numerical-relativity simulation of BH-NS mergers. Here, the presence of strong magnetic fields is one of the most characteristic properties of NSs [28]. However, the role of the magnetic fields in their merger process is still poorly known.

BH-NS mergers can be subject to tidal disruption, for a broad range of the NS compactness, the mass ratio of BH to NS, and BH spin [4–15]. An accretion torus, expected to be formed around the remnant BH, is subject to the magnetorotational instability (MRI) [29], and thus, the magnetic field will be amplified. Previously, it was difficult to perform high resolution simulations to resolve the fastest growing mode of the MRI because of limited computational resources, although several preliminary numerical-relativity simulations have been carried out [30–34].

In this paper, we report the results of our latest general relativistic magnetohydrodynamics (GRMHD) simulation for the BH-NS merger performed on Japanese supercomputer K. The highest-resolution simulation performed so far together with an in-depth resolution study was done.

II. METHOD, INITIAL MODELS, AND GRID SETUP

Einstein's equation is solved in a puncture-Baumgarte-Shapiro-Shibata-Nakamura formalism together with fourth-order finite differencing [35–38] and the GRMHD equations are solved by a high resolution shock capturing scheme. The simulations are performed using a fixed-mesh refinement algorithm in which each refinement level labeled by i covers the cubic domain of $x_{(i)} \in [-N\Delta x_{(i)}, N\Delta x_{(i)}]$ with $\Delta x_{(i)}$ being the grid spacing of level i. $\Delta x_{(i)} = 2\Delta x_{(i+1)}$ and $i = 1, 2 \ldots$, and $i_{max} - 1$ (see Refs. [39,40] for details). Typically, we set $i_{max} = 10$ and the finest grid domain is a $(123 \text{ km})^3$ cube. To examine how the result depends on the grid resolution, we change $\Delta x_{i_{max}} = 120, 160, 202$, and 270 m, respectively. We show

TABLE I.   Grid setup for four different grid-resolution runs. i_{max}: The number of the refinement levels. $\Delta x_{(i_{max})}$: The grid spacing of the finest refinement level. N: The grid number in one positive direction.

Model	i_{max}	$\Delta x_{(i_{max})}$ [m]	N
High	10	120	514
Middle	10	160	378
Normal	8	202	306
Low	8	270	224

the grid setup in our simulations in Table I. In the highest-resolution run, we use 32,768 CPUs.

As initial data, we prepare a BH-NS binary in quasi-quilibrium using the method of Ref. [41]. We model the NS by the Akmal-Pandhalipande-Ravenhall equation of state (EOS) [42], which is compatible with a maximum neutron star mass $\geq 2M_{\odot}$ as required by current observational constraints [43,44]. We set the NS mass, the mass ratio of BH to NS, and the dimensionless aligned spin of BH, χ, to be $1.35M_{\odot}$, 4, and 0.75, respectively. The initial orbital angular velocity is $Gm_0\Omega/c^3 = 0.056$, where G is the gravitational constant, m_0 is the sum of BH and NS gravitational mass in isolation, and c is the speed of light. With these parameters, a massive accretion torus is formed after tidal disruption [8,25].

The initial magnetic-field configuration is given in terms of the vector potential as [45]

$$A_j = (-(y - y_{NS})\delta_j^x + (x - x_{NS})\delta_j^y)A_b \max(P - P_c, 0)^2,$$

where x_{NS} and y_{NS} denote the coordinate center of the NS, P is the pressure, $P_c = P(\rho = 0.04\rho_{max})$, and $j = x, y$, and z. ρ_{max} is the maximum rest-mass density and we set A_b such that the initial maximum magnetic-field strength is 10^{15} G. Even if we start a simulation with this *ad hoc* localized seed magnetic field, the resulting torus surrounding the remnant BH comes to be in a turbulencelike state and a global magnetic field is naturally formed eventually.

The magnetic-field strength is chosen so that the wavelength of the fastest growing mode of the nonaxisymmetric MRI is larger than $10\Delta x_{imax}$. We note that the resulting turbulencelike state should not depend critically on the initial magnetic-field configuration and strength as long as the MRI is resolved [46] (see also Ref. [47] for the discussion of the dependence of the saturation amplitude on the initial field configuration). The EOS is parametrized by a piecewise polytrope [48] and a gamma-law EOS is added during the simulation to capture shock heating effects with thermal gamma of 1.8. Another choice of thermal gamma could affect the amount of the torus wind.

III. RESULTS

Figure 1 shows snapshots of the rest-mass density profile with the magnetic-field lines. Before swallowed by the BH, the NS is tidally disrupted. A part of NS matter subsequently forms an accretion torus around the remnant BH with mass of $\approx 0.13M_{\odot}$ at ≈ 10 ms after the tidal disruption. The Kelvin-Helmholtz instability develops in the contact interfaces of the wound spiral arm because of the presence of shear motion shown in Fig. 1(a) and the vortices are generated subsequently enhancing the magnetic-field energy. In addition, the nonaxisymmetric MRI activates amplification of the magnetic-field strength [49] [Fig. 1(b)]. The mass accretion is enhanced by turbulencelike motion that is generated by these magnetohydrodynamics (MHD) instabilities as well as by the gravitational torque exerted by the nonaxisymmetric structure of the accretion torus [see Fig. 1(c) and visualization in Ref. [50]].

Figure 2 plots the ejecta mass, torus mass, mass accretion rate onto the BH, and ratio of the magnetic-field energy, E_B, to internal energy, E_{int}, as functions of time. We define the merger time t_{mrg} to be the time at which the gravitational-wave amplitude becomes maximal. The ejecta are defined to be fluid elements that reside outside the BH and have $u_t < -1$ where u_t is the lower time component of the four velocity. This criterion means that the fluid elements are gravitationally unbounded. The primary
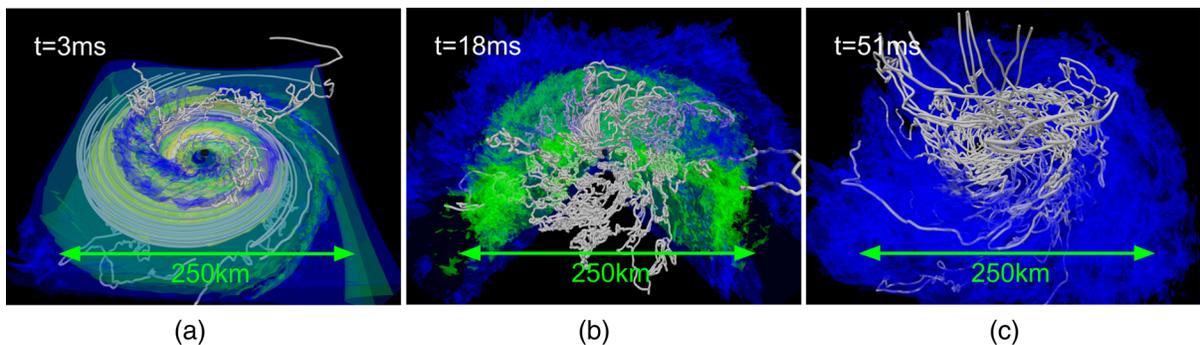

FIG. 1 (color online).   Snapshots of the rest-mass density profile with the magnetic-field lines (a) just after tidal disruption, (b) at an early phase of accretion torus, and (c) in the final phase. The isosurfaces for 10^{11}, 10^{10}, and 10^9 g/cm^3 are denoted by yellow, green, and blue. The magnetic-field lines are shown by the white curves. In the middle panel, the isosurfaces are drawn for the three-quarter region.
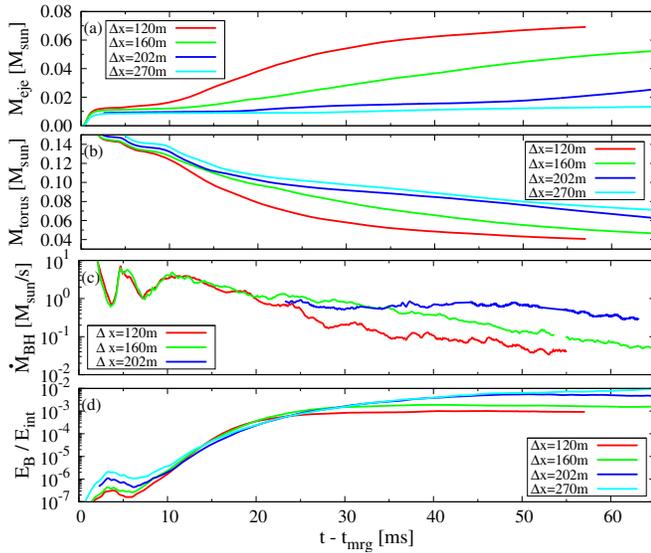
FIG. 2 (color online). Time evolution of (a) ejecta mass, (b) torus mass, (c) mass accretion rate onto the BH, and (d) magnetic-field energy divided by internal energy. In panel (c), the data for $t - t_{\mathrm{mrg}} \lesssim 20$ ms for $\Delta x = 202$ m run is not plotted.
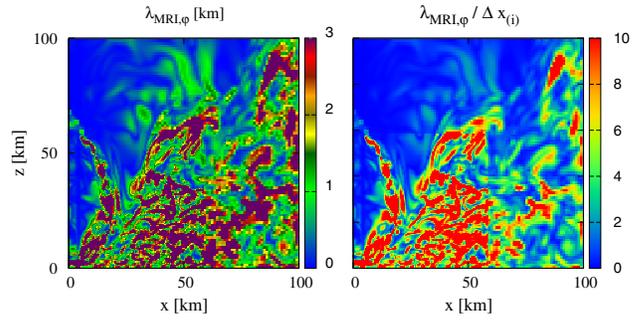

FIG. 3 (color online). Profiles of wavelength of the fastest growing mode for nonaxisymmetric MRI (left) and the wavelength divided by the grid resolution (right) on a meridional plane (x-z) at $t - t_{\mathrm{mrg}} \approx 15.0$ ms for the lowest-resolution run.

mass-ejection mechanism is tidal torque exerted during tidal disruption and these *dynamical* ejecta are seen for 0 ms $\lesssim t - t_{\mathrm{mrg}} \lesssim 10$ ms in Fig. 2. During this early phase, NS matter of $\sim 0.01 M_{\odot}$ is ejected approximately along the orbital plane. This result agrees with that found in Refs. [7,8], which demonstrates that our findings will remain robust also for a larger initial separation.

After this primary phase, a new ejecta component appears. In the highest-resolution run, the accumulated accretion mass onto the BH for 10 ms $\lesssim t - t_{\mathrm{mrg}} \lesssim 30$ ms is $\approx 0.03 M_{\odot}$, while the torus mass decreases by $\approx 0.06 M_{\odot}$ over the same time. This implies that a significant amount of the torus mass is ejected by a torus wind. The launch time and amount of material ejected by the wind depend strongly on the grid resolution: The higher resolution runs result in an earlier launch time and larger amount of the ejecta. The mass accretion rate onto the BH also depends on the grid resolution: For higher resolutions, it is smaller. The reason for these facts will be described later.

The bottom panel of Fig. 2 shows that irrespective of the grid resolution, the magnetic-field energy is exponentially enhanced and eventually saturated: E_B is typically 0.1% of E_{int}. The growth rates of E_B for 10 ms $\lesssim t - t_{\mathrm{mrg}} \lesssim 20$ ms correspond to 7–8% of the orbital angular velocity. This growth rate agrees approximately with that of the non-axisymmetric MRI predicted by the linear perturbation analysis [49].

To see that our grid setting is sufficient to resolve the fastest growing mode of the nonaxisymmetric MRI, Fig. 3 plots a snapshot of wavelength of the fastest growing mode

of the nonaxisymmetric MRI on a meridional (x-z) plane at $t - t_{\mathrm{mrg}} \approx 15.0$ ms. We estimate the wavelength by

$$\lambda_{\mathrm{MRI},\varphi} = \frac{b_{(\varphi)}}{\sqrt{4\pi\rho h + b^{\mu} b_{\mu}}} \frac{2\pi}{\Omega},$$

where $b_{(\varphi)}$, ρ, h, and Ω are an azimuthal component of the magnetic field measured in the fluid rest frame, the rest-mass density, the specific enthalpy, and the angular velocity, respectively. The wavelength is longer than ≈ 3 km in a large portion of the region and this indicates the fastest growing mode is covered by more than ten grid points even in the lowest-resolution run. The right panel of Fig. 3 clearly shows it. Therefore, turbulencelike motion produced by the MRI, which is resolved in our numerical simulation, plays an important role in the mass ejection. We discuss this point later.

In the presence of neutrino radiation, the growth rate of the fastest growing MRI mode could be significantly suppressed once neutrino viscosity and drag turn on [51]. According to Ref. [51], the neutrino viscosity ν, the neutrino mean free path $\lambda_{\nu-\mathrm{mfp}}$, and the wavelength of the fastest growing MRI mode $\lambda_{\mathrm{vis\text{-}MRI}}$ in the viscous regime are

$$\nu = 1.2 \times 10^{12} T_{10}^2 \rho_{12}^{-2} \text{ cm}^2 \text{ s}^{-1},$$

$$\lambda_{\nu-\mathrm{mfp}} = 10^5 \rho_{12}^{-1} T_{10}^{-2} \text{ cm},$$

$$\lambda_{\mathrm{vis\text{-}MRI}} = 2.4 \times 10^5 \Omega_3^{-1/2} \nu_{12}^{1/2} \text{ cm},$$

where $T_{10} = T/10$ MeV, $\rho_{12} = \rho/10^{12}$ g cm^{-3}, $\Omega_3 = \Omega/10^3$ s^{-1}, and $\nu_{12} = \nu/10^{12}$ cm^2 s^{-1}. Note that these estimates would depend on the structure of the accretion torus [52,53].

Assuming the gas, photons, and relativistic electron and positrons contribute to the specific thermal energy, we evaluate the temperature from the thermal component of the specific internal energy [54]. We utilize the data of the
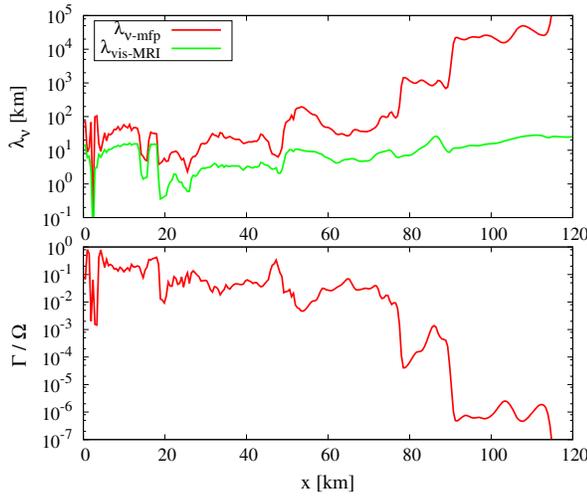
FIG. 4 (color online). (Top) Radial profile of the neutrino mean free path and the wavelength of the fastest growing MRI mode in the viscous region. The BH resides at the origin. (Bottom) Radial profile of the damping rate.
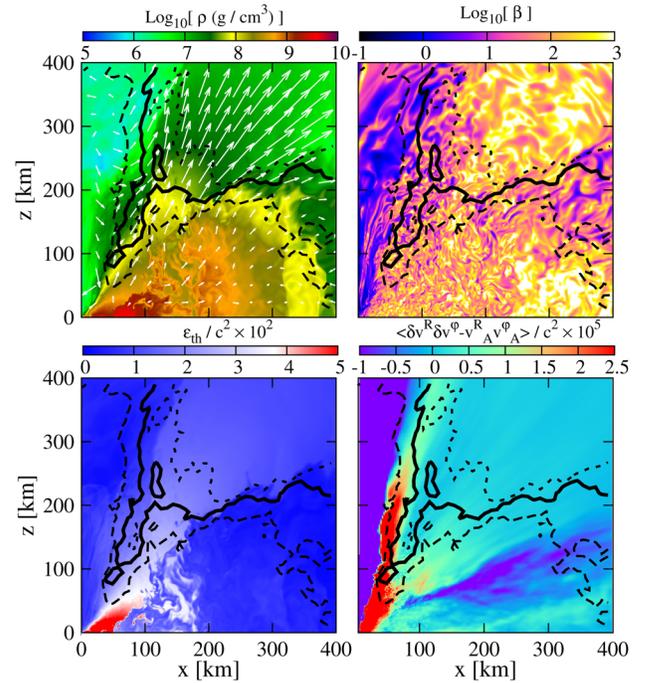

FIG. 5 (color online). Profiles of rest-mass density with velocity fields (top left), plasma β (top right), the thermal component of specific internal energy (bottom-left), and the sum of the Maxwell and Reynolds stress (bottom right) on the meridional plane at $t - t_{\text{mrg}} \approx 50.6$ ms for the highest-resolution run. In all the panels, the black curves denote contours with $u_t = -0.98$ (dashed), -1.00 (solid), and -1.02 (dotted), respectively. In the bottom-right panel, the red (purple) colored region indicates that the energy is transferred outward (inward).

density, angular velocity, and the specific internal energy along the x axis on the equatorial plane at $t - t_{\text{mrg}} \approx 10$ ms.

Figure 4 plots the radial profile of $\lambda_{\nu-\text{mfp}}$ and $\lambda_{\text{vis-MRI}}$. In the entire region, $\lambda_{\nu-\text{mfp}}$ is always longer than $\lambda_{\text{vis-MRI}}$, which implies that the effect of neutrinos on the MRI is not described by the viscosity, but by the neutrino drag. The neutrino drag is characterized by the damping rate Γ of the velocity fluctuation due to the momentum transport. According to Ref. [51], $\Gamma = 6 \times 10^3 T_{10}^6$ s^{-1}. The radial profile of Γ is shown in Fig. 4. Because $\Gamma \ll \Omega$ in the entire region, the growth rate of the MRI is not affected by the neutrino drag. Although there is an ambiguity in terms of the accretion torus structure and the temperature estimation, we conclude that the MRI growth rate is not significantly different from that of the ideal MHD in this BH-NS merger. The MRI will grow exponentially even if we assume a weak magnetic-field strength of $\sim 10^{11}$ G.

Figure 5 plots snapshots of the rest-mass density, plasma β (the ratio of matter pressure to magnetic pressure), thermal component of specific internal energy, and sum of the Maxwell and Reynolds stress on the x-z plane at $t - t_{\text{mrg}} \approx 50.6$ ms for the highest-resolution run. We also plot contours of u_t. Here, $W \equiv \ln(-u_t)$ is an effective potential of a test particle moving in stationary and axisymmetric BH spacetime [55]. The shape of curves in the vicinity of the rotational axis with $u_t = -1$ is approximately parabolic. In the Newtonian limit, W is reduced to $-GM_{\text{BH}}/(R^2 + z^2)^{1/2} + l^2/2R^2$ where M_{BH}, R, and l are the BH mass, cylindrical coordinate, and specific angular momentum, respectively. We assume constant specific angular momentum for simplicity. In this case, for a given value of l the contour of $u_t = -1$ becomes parabolic. If the specific angular momentum for fluid elements is sufficiently enhanced or fluid elements are pushed to high

latitude $(z \gtrsim R)$ by thermal pressure, they could have $u_t \leq -1$ $(W \geq 0)$ [56–58] (see the discussion in the next paragraph). Because there is no matter in the region above the torus, the wind, once it is launched, expands in the widely spread radial direction by contrast with the tidally induced ejecta. Subsequently, a funnel wall is formed.

The point to be clarified is how fluid elements are injected into the region with $u_t < -1$ $(W > 0)$. We find that β at the launch time of the wind is much greater than unity near the torus; pure magnetic pressure would not be the main agent of the injection. The bottom-left panel of Fig. 5 indicates that there is a hot region in the vicinity of the BH, which produces a steep pressure gradient. Because of this gradient, the fluid elements are accelerated radially and become unbound once they reach the region with $u_t < -1$ $(W > 0)$ (see Ref. [56] for essentially the same discussion).

To explore the mechanism to enhance the thermal pressure, we analyze the specific kinetic-energy spectrum $E(k)$, which is calculated by $1/2 \int \int_V \sum_j e^{-i\vec{k} \cdot \vec{r}} \langle \delta v^j(\vec{x} + \vec{r}) \delta v^j(\vec{x}) \rangle d^3 r d\Omega_k$ where $\vec{k}$ is a wave number vector, $k = |\vec{k}|$, $d\Omega_k$ is the volume element in a spherical shell between k and $k + dk$, and V is a cubic region of $x[\text{km}] \in [50, 70]$, $y[\text{km}] \in [-10, 10]$, $z[\text{km}] \in [-10, 10]$. We choose $\vec{x}$ as the
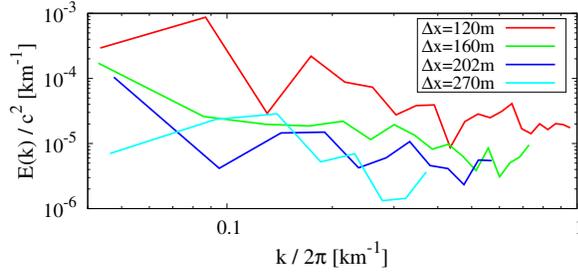
FIG. 6 (color online). Energy spectrum of the matter flow in all runs.

center of the cube and $\vec{r}$ is the position vector from the center. The fluctuation of the velocity δv^i is $v^i - \langle v^i \rangle$ inside the chosen cube. $\langle \cdot \rangle$ denotes the time average for the duration $10 \text{ ms} \le t - t_{\mathrm{mrg}} \le 20 \text{ ms}$.

Figure 6 plots this energy spectrum for all runs. This shows that (i) the spectrum is extended to smaller scales in the higher resolution runs, indicating that the energy is injected at a small scale at which the MRI develops and (ii) the spectrum amplitude is higher for the higher resolution runs. Numerically resolvable wavelength of the fastest growing mode of the MRI becomes shorter by increasing the grid resolution. Therefore, the wave number for which the MRI develops is given by $k/2\pi = 1/10\Delta x_{\mathrm{imax}} \approx 0.83 \text{ km}^{-1}$ for the highest-resolution run, $\approx 0.62 \text{ km}^{-1}$ for the middle-resolution run, $\approx 0.50 \text{ km}^{-1}$ for the normal-resolution run, and $\approx 0.33 \text{ km}^{-1}$ for the lowest-resolution run, respectively. This is expected to be approximately equal to the energy injection scale in $E(k)$. Assuming that a turbulent state is realized, the specific energy dissipation rate is $\sim \delta v^3 / l_{\mathrm{edd}}$ where l_{edd} is the scale of the vortices [59]. Because the turbulent energy is proportional to δv^2, Fig. 6 suggests that δv becomes higher in the higher resolution runs for a given scale l_{edd}. This indicates that the effective turbulent viscosity, $l_{\mathrm{edd}}\delta v$, increases with increasing resolution. Because of the realistic high viscosity achieved by this turbulencelike motion, the mass accretion inside the accretion torus is enhanced in the higher resolution runs and the mass accretion energy is
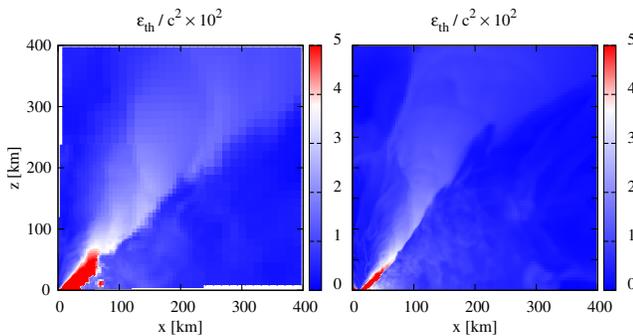
efficiently converted to thermal energy in the vicinity of the BH [60–62].

Figure 7 plots snapshots of the thermal component of specific internal energy on the x-z plane at $t - t_{\mathrm{mrg}} \approx 50.6 \text{ ms}$ for $\Delta x = 160$ and 270 m. Comparing to the bottom-left panel of Fig. 5, the thermal component of specific internal energy in the vicinity of the inner edge of the torus and the torus interior is larger than that in the rest of the torus in the higher resolution run. This trend indicates that efficient thermalization of the mass accretion energy due to the effective turbulent viscosity would be realized as discussed above. Consequently, the torus-wind power is enhanced while the mass accretion onto the BH is suppressed [60–62], which can be seen clearly in Fig. 2. The bottom-right panel of Fig. 5 indeed shows that the energy is transferred outward. In Figs. 2 and 6, the amount of the ejecta mass and the spectrum of the matter flow do not exhibit the convergence. However, with the improvement of the grid resolution, the total amount of the torus-wind mass increases and this indicates that our highest-resolution results would show the lower bound of the total wind mass.

The high BH spin with a small horizon radius, which is necessary for tidal disruption of realistic BH-NS binaries [8,10–14], prevents the fluid elements from being accreted on the remnant BH. Then the fluid elements tend to stay in the vicinity of the BH and the pressure gradient is enhanced [63]. This is also the key to pushing the fluid elements outward [56]. In our simulation, the BH is spun up to $\chi \approx 0.9$, which implies the radius of the innermost stable circular orbit is so small, $\approx 2.32 GM_{\mathrm{BH}}/c^2$ [64], that an efficient draining by the BH is prohibited. Hence, the accretion onto the BH is suppressed [63,65] [see also panel (c) of Fig. 2]. The amount of the torus-wind mass is $\approx 0.06 M_\odot$ in the highest-resolution run, which corresponds to about 50% of the torus mass at $t - t_{\mathrm{mrg}} \approx 10 \text{ ms}$.

As discussed above, the pressure gradient in the vicinity of the BH accelerates the outflow and this results in the formation of coherent poloidal magnetic fields because the magnetic-field lines are frozen into fluid elements. A low-β

FIG. 7 (color online). Profiles of the thermal component of specific internal energy for $\Delta x = 160$ m (left) and $\Delta x = 270$ m (right) on a meridional (x-z) plane at $t - t_{\mathrm{mrg}} \approx 50.6 \text{ ms}$.
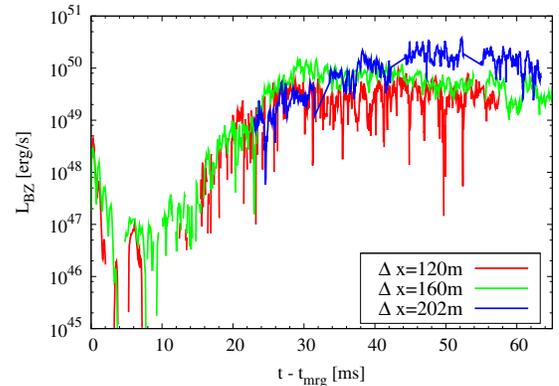

FIG. 8 (color online). Time evolution of outgoing Poynting flux estimated on an apparent horizon.

region is formed along the funnel wall in the wind phase. Subsequently, the magnetic pressure pushes matter and magnetic-field lines to the polar region because there is only dilute matter in this region at the wind launch. This results in the formation of a BH magnetosphere. The top-right panel of Fig. 5 indeed shows that a region with $\beta \sim 10^{-1}$ is formed around the z axis. In the presence of a BH magnetosphere composed of a coherent poloidal magnetic field, the Blandford-Znajek (BZ) mechanism [66] efficiently works for the outgoing Poynting flux generation. Figure 8 plots time evolution of the outgoing Poynting flux estimated on an apparent horizon. This figure shows that the Poynting flux is significantly enhanced after the wind launch because of the coherent poloidal magnetic-field formation. The Poynting flux is as high as $\approx 2 \times 10^{49}$ erg/s in the end of the highest-resolution run.

IV. SUMMARY AND DISCUSSION

We performed high resolution GRMHD simulations of a BH-NS merger on the supercomputer K. We self-consistently show a series of the processes composed of tidal disruption of the NS, the accretion torus formation, the magnetic-field amplification due to the nonaxisymmetric MRI, thermally driven torus wind, subsequent formation of the funnel wall and BH magnetosphere, and the high BZ luminosity.

A resolution study revealed that turbulencelike motion works as the agent to drive the mass accretion and convert kinetic energy to thermal energy resulting in the generation of a strong wind. To show this phenomenon, sufficiently high resolution simulations are essential. After the launch of the torus wind, a funnel wall and magnetosphere with collimated poloidal magnetic fields are naturally formed.

The torus wind and subsequent funnel plus magnetosphere formation have the following implications. First, the formed magnetosphere could help launch a jet by the BZ mechanism. The high outgoing Poynting flux found in our simulation could be the main engine for sGRBs [67]. Also, the jet could be collimated naturally by the pressure exerted by the funnel wall once the wind is launched.

The torus wind could contribute significantly to r-process nucleosynthesis of heavy elements in BH-NS mergers. The dynamical ejecta would be neutron rich and have a low value of electron fraction Y_e. By contrast, the torus-wind component is expected to have a higher value of Y_e due to weak interactions because it has a high temperature by shock heating [68]. A mixture of the dynamical and wind components could be key to reproducing the solar abundance pattern of the r-process heavy elements. Note that it was suggested that viscosity-driven and neutrino-driven winds from a torus around the BH could reproduce the solar abundances for a mass number greater than 90 [68] (see also Refs. [69,70] for the NS-NS case).

Finally, we comment on the kilonova/macronova (radioactively powered electromagnetic emission) model [18]. The amount of the torus-wind component in the highest-resolution run is as high as $\approx 0.06 M_\odot$, which is much larger than that of the dynamical component $\approx 0.01 M_\odot$. The torus wind would significantly contribute to kilonova/macronova in BH-NS mergers. This point should be investigated systematically in a future work.

ACKNOWLEDGMENTS

[1] J. Abadie *et al.*, Calibration of the LIGO gravitational wave detectors in the fifth science run, Nucl. Instrum. Methods Phys. Res., Sect. A **624**, 223 (2010).

[2] T. Accadia *et al.*, Calibration and sensitivity of the Virgo detector during its second science run, Classical Quantum Gravity **28**, 025005 (2011); **28**, 079501 (2011).

[3] K. Kuroda, Status of LCGT, Classical Quantum Gravity **27**, 084004 (2010).

[4] M. Shibata, K. Kyutoku, T. Yamamoto, and K. Taniguchi, Gravitational waves from black hole-neutron star binaries I: classification of waveforms, Phys. Rev. D **79**, 044030 (2009); **85**, 127502 (2012).

[5] K. Kyutoku, M. Shibata, and K. Taniguchi, Gravitational waves from nonspinning black hole-neutron star binaries: dependence on equations of state, Phys. Rev. D **82**, 044049 (2010); **84**, 049902 (2011).

[6] K. Kyutoku, H. Okawa, M. Shibata, and K. Taniguchi, Gravitational waves from spinning black hole-neutron star binaries: dependence on black hole spins and on neutron star equations of state, Phys. Rev. D 84, 064018 (2011).

[7] K. Kyutoku, K. Ioka, and M. Shibata, Anisotropic mass ejection from black hole-neutron star binaries: diversity of electromagnetic counterparts, Phys. Rev. D 88, 041503 (2013).

[8] K. Kyutoku, K. Ioka, H. Okawa, M. Shibata, and K. Taniguchi, Dynamical mass ejection from black hole-neutron star binaries, Phys. Rev. D 92, 044028 (2015).

[9] F. Foucart, E. O'Connor, L. Roberts, M. D. Duez, R. Haas, L. E. Kidder, C. D. Ott, H. P. Pfeiffer, M. A. Scheel, and B. Szilagyi, Postmerger evolution of a neutron star-black hole binary with neutrino transport, Phys. Rev. D 91, 124021 (2015).

[10] F. Foucart, M. B. Deaton, M. D. Duez, E. O'Connor, C. D. Ott, R. Haas, L. E. Kidder, H. P. Pfeiffer, M. A. Scheel, and B. Szilagyi, Neutron star-black hole mergers with a nuclear equation of state and neutrino cooling: dependence in the binary parameters, Phys. Rev. D 90, 024026 (2014).

[11] M. B. Deaton, M. D. Duez, F. Foucart, E. O'Connor, C. D. Ott, L. E. Kidder, C. D. Muhlberger, M. A. Scheel, and B. Szilagyi, Black hole-neutron star mergers with a hot nuclear equation of state: outflow and neutrino-cooled disk for a low-mass, high-spin case, Astrophys. J. 776, 47 (2013).

[12] G. Lovelace, M. D. Duez, F. Foucart, L. E. Kidder, H. P. Pfeiffer, M. A. Scheel, and B. Szilgyi, Massive disc formation in the tidal disruption of a neutron star by a nearly extremal black hole, Classical Quantum Gravity 30, 135004 (2013).

[13] F. Foucart, M. D. Duez, L. E. Kidder, M. A. Scheel, B. Szilagyi, and S. A. Teukolsky, Black hole-neutron star mergers for ten solar mass black holes, Phys. Rev. D 85, 044015 (2012).

[14] F. Foucart, M. B. Deaton, M. D. Duez, L. E. Kidder, I. MacDonald, C. D. Ott, H. P. Pfeiffer, M. A. Scheel et al., Black hole-neutron star mergers at realistic mass ratios: equation of state and spin orientation effects, Phys. Rev. D 87, 084006 (2013).

[15] F. Foucart, M. D. Duez, L. E. Kidder, and S. A. Teukolsky, Black hole-neutron star mergers: effects of the orientation of the black hole spin, Phys. Rev. D 83, 024005 (2011).

[16] R. Narayan, B. Paczynski, and T. Piran, Gamma-ray bursts as the death throes of massive binary stars, Astrophys. J. 395, L83 (1992).

[17] J. M. Lattimer and D. N. Schramm, Black-hole-neutron-star collisions, Astrophys. J. 192, L145 (1974).

[18] L.-X. Li and B. Paczynski, Transient events from neutron star mergers, Astrophys. J. 507, L59 (1998).

[19] B. D. Metzger and E. Berger, What is the most promising electromagnetic counterpart of a neutron star binary merger? Astrophys. J. 746, 48 (2012).

[20] T. Piran, E. Nakar, and S. Rosswog, The electromagnetic signals of compact binary mergers, Mon. Not. R. Astron. Soc. 430, 2121 (2013).

[21] S. Rosswog, T. Piran, and E. Nakar, The multimessenger picture of compact object encounters: binary mergers versus dynamical collisions, Mon. Not. R. Astron. Soc. 430, 2585 (2013).

[22] R. Fernndez and B. D. Metzger, Delayed outflows from black hole accretion tori following neutron star binary coalescence, Mon. Not. R. Astron. Soc. 435, 502 (2013).

[23] A. Bauswein, R. Ardevol Pulpillo, H. T. Janka, and S. Goriely, Nucleosynthesis constraints on the neutron star-black hole merger rate, Astrophys. J. 795, L9 (2014).

[24] K. Hotokezaka, K. Kyutoku, M. Tanaka, K. Kiuchi, Y. Sekiguchi, M. Shibata, and S. Wanajo, Progenitor models of the electromagnetic transient associated with the short gamma ray burst 130603B, Astrophys. J. 778, L16 (2013).

[25] M. Tanaka, K. Hotokezaka, K. Kyutoku, S. Wanajo, K. Kiuchi, Y. Sekiguchi, and M. Shibata, Radioactively powered emission from black hole-neutron star mergers, Astrophys. J. 780, 31 (2014).

[26] H. Takami, T. Nozawa, and K. Ioka, Dust formation in macronovae, Astrophys. J. 789, L6 (2014).

[27] S. Kisaka, K. Ioka, and H. Takami, Energy sources and light curves of macronovae, Astrophys. J. 802, 119 (2015).

[28] R. N. Manchester, G. B. Hobbs, A. Teoh, and M. Hobbs, The Australia telescope national facility pulsar catalogue, Astron. J. 129, 1993 (2005).

[29] S. A. Balbus and J. F. Hawley, A powerful local shear instability in weakly magnetized disks. 1. Linear analysis. 2. Nonlinear evolution, Astrophys. J. 376, 214 (1991).

[30] Y. T. Liu, S. L. Shapiro, Z. B. Etienne, and K. Taniguchi, General relativistic simulations of magnetized binary neutron star mergers, Phys. Rev. D 78, 024012 (2008).

[31] Z. B. Etienne, Y. T. Liu, V. Paschalidis, and S. L. Shapiro, General relativistic simulations of black hole-neutron star mergers: effects of magnetic fields, Phys. Rev. D 85, 064029 (2012).

[32] Z. B. Etienne, V. Paschalidis, and S. L. Shapiro, General relativistic simulations of black hole-neutron star mergers: effects of tilted magnetic fields, Phys. Rev. D 86, 084026 (2012).

[33] S. Chawla, M. Anderson, M. Besselman, L. Lehner, S. L. Liebling, P. M. Motl, and D. Neilsen, Mergers of Magnetized Neutron Stars with Spinning Black Holes: Disruption, Accretion, and Fallback, Phys. Rev. Lett. 105, 111101 (2010).

[34] V. Paschalidis, M. Ruiz, and S. L. Shapiro, Relativistic simulations of black hole-neutron star coalescence: the jet emerges, Astrophys. J. 806, L14 (2015).

[35] M. Shibata and T. Nakamura, Evolution of three-dimensional gravitational waves: Harmonic slicing case, Phys. Rev. D 52, 5428 (1995).

[36] T. W. Baumgarte and S. L. Shapiro, numerical integration of Einstein's field equations, Phys. Rev. D 59, 024007 (1998).

[37] M. Campanelli, C. O. Lousto, P. Marronetti, and Y. Zlochower, Accurate Evolutions of Orbiting Black-Hole Binaries without Excision, Phys. Rev. Lett. 96, 111101 (2006).

[38] J. G. Baker, J. Centrella, D.-I. Choi, M. Koppitz, and J. van Meter, Gravitational-Wave Extraction from an Inspiraling Configuration of Merging Black Holes, Phys. Rev. Lett. 96, 111102 (2006).

[39] K. Kiuchi, K. Kyutoku, and M. Shibata, Three-dimensional evolution of differentially rotating magnetized neutron stars, Phys. Rev. D 86, 064008 (2012).

[40] K. Kiuchi, K. Kyutoku, Y. Sekiguchi, M. Shibata, and T. Wada, High resolution numerical relativity simulations for

the merger of binary magnetized neutron stars, Phys. Rev. D **90**, 041502(R) (2014).

[41] K. Kyutoku, M. Shibata, and K. Taniguchi, Quasiequilibrium states of black hole-neutron star binaries in the moving-puncture framework, Phys. Rev. D **79**, 124018 (2009).

[42] A. Akmal, V. R. Pandharipande, and D. G. Ravenhall, Equation of state of nucleon matter and neutron star structure, Phys. Rev. C **58**, 1804 (1998).

[43] P. Demorest, T. Pennucci, S. Ransom, M. Roberts, and J. Hessels, A two-solar-mass neutron star measured using Shapiro delay, Nature (London) **467**, 1081 (2010).

[44] J. Antoniadis, P. C. C. Freire, N. Wex, T. M. Tauris, R. S. Lynch, M. H. van Kerkwijk, M. Kramer, C. Bassa *et al.*, A massive pulsar in a compact relativistic binary, Science **340**, 1233232 (2013).

[45] M. Shibata, M. D. Duez, Y. T. Liu, S. L. Shapiro, and B. C. Stephens, Magnetized Hypermassive Neutron Star Collapse: A Central Engine for Short Gamma Ray Bursts, Phys. Rev. Lett. **96**, 031102 (2006).

[46] S. A. Balbus and J. F. Hawley, Instability, turbulence, and enhanced transport in accretion disks, Rev. Mod. Phys. **70**, 1 (1998).

[47] M. Obergaulinger, M. A. Aloy, and E. Muller, Local simulations of the magnetized Kelvin-Helmholtz instability in neutron-star mergers, Astron. Astrophys. **515**, A30 (2010).

[48] J. S. Read, B. D. Lackey, B. J. Owen, and J. L. Friedman, Constraints on a phenomenologically parametrized neutron-star equation of state, Phys. Rev. D **79**, 124032 (2009).

[49] S. A. Balbus and J. F. Hawley, A powerful local shear instability in weakly magnetized disks. IV. Nonaxisymmetric perturbations, Astrophys. J. **400**, 610 (1992).

[50] K. Kiuchi, http://www2.yukawa.kyoto-u.ac.jp/~kenta .kiuchi/GWRC/.

[51] J. Guilet, E. Mueller, and H. T. Janka, Neutrino viscosity and drag: impact on the magnetorotational instability in protoneutron stars, Mon. Not. R. Astron. Soc. **447**, 3992 (2015).

[52] Y. Masada, T. Sano, and K. Shibata, The effect of neutrino radiation on magnetorotational instability in protoneutron stars, Astrophys. J. **655**, 447 (2007).

[53] T. A. Thompson, E. Quataert, and A. Burrows, Viscosity and rotation in core-collapse supernovae, Astrophys. J. **620**, 861 (2005).

[54] M. Shibata and K. Taniguchi, Merger of black hole and neutron star in general relativity: tidal disruption, torus mass, and gravitational waves, Phys. Rev. D **77**, 084015 (2008).

[55] C. W. Misner, K. S. Thorne, and J. A. Wheeler, *Gravitation* (W. H. Freeman and Company, New York, 1973).

[56] J. F. Hawley and J. H. Krolik, Magnetically driven jets in the Kerr metric, Astrophys. J. **641**, 103 (2006).

[57] R. D. Blandford and M. C. Begelman, On the fate of gas accreting at a low rate onto a black hole, Mon. Not. R. Astron. Soc. **303**, L1 (1999).

[58] J. M. Stone and J. E. Pringle, Magnetohydrodynamical nonradiative accretion flows in two dimensions, Mon. Not. R. Astron. Soc. **322**, 461 (2001).

[59] L. D. Landau and E. M. Lifshitz, *Fluid Mechanics* (Pergamon Press, Oxford, 1984).

[60] Z. Kuncic and G. V. Bicknell, Dynamics and energetics of turbulent, magnetized disk accretion around black holes: a first-principles approach to disk-corona-outflow coupling, Astrophys. J. **616**, 669 (2004).

[61] D. Maruta and O. Kaburaki, Viscosity-driven winds from magnetized accretion disks, Astrophys. J. **593**, 85 (2003).

[62] I. V. Igumenshchev and M. A. Abramowicz, Two-dimensional models of hydrodynamical accretion flows into black holes, Astrophys. J. Suppl. Ser. **130**, 463 (2000).

[63] M. Shibata, Y. Sekiguchi, and R. Takahashi, Magnetohydrodynamics of neutrino-cooled accretion tori around a rotating black hole in general relativity, Prog. Theor. Phys. **118**, 257 (2007).

[64] S. L. Shapiro and S. A. Teukolsky, *Black holes, White Dwarfs, and Neutron Stars* (Wiley-VCH, Berlin, 1983).

[65] C. F. Gammie, S. L. Shapiro, and J. C. McKinney, Black hole spin evolution, Astrophys. J. **602**, 312 (2004).

[66] R. D. Blandford and R. L. Znajek, Electromagnetic extractions of energy from Kerr black holes, Mon. Not. R. Astron. Soc. **179**, 433 (1977).

[67] W. H. Lee and E. Ramirez-Ruiz, The progenitors of short gamma ray bursts, New J. Phys. **9**, 17 (2007).

[68] O. Just, A. Bauswein, R. A. Pulpillo, S. Goriely, and H.-T. Janka, Comprehensive nucleosynthesis analysis for ejecta of compact binary mergers, Mon. Not. R. Astron. Soc. **448**, 541 (2015).

[69] S. Wanajo, Y. Sekiguchi, N. Nishimura, K. Kiuchi, K. Kyutoku, and M. Shibata, Production of all the *r*-process nuclides in the dynamical ejecta of neutron star mergers, Astrophys. J. **789**, L39 (2014).

[70] Y. Sekiguchi, K. Kiuchi, K. Kyutoku, and M. Shibata, The dynamical mass ejection from binary neutron star mergers: radiation-hydrodynamics study in general relativity, Phys. Rev. D **91**, 064059 (2015).